JOURNAL OF PROPULSION AND POWER
Vol. 19, No. 2, March–April 2003

Numerical Simulation of High-Pressure and Fuel-Rich Turbulent Combustion Field

Takurou Makita,* Takahisa Yamamoto,† Tomohiko Furuhata,‡ and Norio Arai§
Nagoya University, Nagoya 464-8603, Japan

To obtain fundamental data to design a practical gas turbine combustor in a chemical gas turbine combined system, a methane–air turbulent diffusion combustor under high-pressure and fuel-rich conditions has been simulated. As a reaction model, the assumed probability density function (PDF) model based on the calculated results of a counterflow diffusion flame and the eddy dissipation concept model with reduced reaction schemes were adopted to predict the turbulent combustion characteristics especially under the fuel-rich condition. These numerical simulations were carried out using a commonly used workstation DEC 500au, and species concentrations and temperature profiles in fuel-rich turbulent diffusion combustor were predicted. Comparisons of the results calculated by both simulation models show quantitative and qualitative discrepancies in unburned species profiles such as CO and H_2. The simulated results of the PDF model shows good agreement with experimental results of not only temperature and burned species profiles but also unburned species profiles. These combustion simulations were completed within 12 h. From the comparisons and discussions, it is concluded that the PDF model could predict the methane–air turbulent diffusion combustion characteristics with accuracy under fuel-rich and high-pressure conditions.

Nomenclature

C_{g1}, C_{g2}	=	g-equation model constant
$C_\mu, C_{\varepsilon 1}, C_{\varepsilon 2}$	=	model constants of k–ε model
D	=	combustor diameter, m
F_x, F_r, F_θ	=	composite radiation flux, W/m^2
f	=	mixture fraction
G_k	=	stress production of k, m^2/s^3
g	=	concentration fluctuations
h	=	enthalpy, kJ/kg
k	=	turbulent kinetic energy, m^2/s^2
L	=	distance between jet planes, m
m_i	=	mass fraction for i
P	=	probability density function
S_ϕ	=	source term for f
U, V, W	=	time mean velocity component, m/s
x, y, z	=	coordinate
x, r, θ	=	cylindrical coordinate
Zc	=	mass fraction for C element
Γ_ϕ	=	diffusion coefficient for f
ε	=	dissipation rate of k, m^2/s^3
μ	=	dynamic viscosity, kg/m/s
ρ	=	density, kg/m^3
$\sigma_k, \sigma_\varepsilon, \sigma_m$	=	effective Schmidt number
$\sigma_h, \sigma_f, \sigma_g$		of subscripted entity
ϕ	=	generalized variable

Subscripts

eff	=	effective
i	=	chemical species
t	=	turbulence
1	=	fuel flow
2	=	airflow

Received 26 June 2001; revision received 10 December 2002; accepted for publication 18 December 2002.

*Graduate Student, Research Center for Advanced Energy Conversion, Furo-cho, Chikusa-ku.

†Ph.D. Student, Research Center for Advanced Energy Conversion, Furo-cho, Chikusa-ku.

‡Research Associate, Research Center for Advanced Energy Conversion, Furo-cho, Chikusa-ku; furu@nuce.nagoya-u.ac.jp.

§Professor, Research Center for Advanced Energy Conversion, Furo-cho, Chikusa-ku.

Introduction

We have proposed a new gas-turbine/steam-turbine combined cycle chemical gas turbine (CGT) system.[1,2] The schematic diagram of the proposed system is shown in Fig. 1. It consists of a fuel-rich combustor, a fuel-lean combustor, two sets of gas turbines, a steam turbine, a recuperator, and heat recovery steam generators. An important feature of this system is the introduction of a fuel stoichiometry manipulation technique with fuel-rich combustion in the first combustor and fuel-lean combustion in the second. When it is considered that the only promising materials for turbine blades operating at temperatures above 1773 K without internal cooling are carbon-fiber-reinforced-carbon(C/C) composites, fuel rich, that is, oxygen-lean, combustion and coating with C/C composites are employed to prevent their deterioration at these high temperatures. The second turbine is operated at temperatures of at most 1723 K, where conventional turbine blade material is used. The system has three features. First, fuel-rich combustion in the first combustor would suppress NOx emissions. Second, the heat resistant materials (including C/C composites) could be used as turbine blades. Third, there is no need for a cooling technique for the turbine blade to decrease exergy loss. According to the system analysis by a process simulator, the total exergy efficiency of this system is 63%, when the equivalence ratio and turbine inlet temperature in the first fuel-rich combustor are set to 1.60 and 1773 K, respectively. It is clear that the first fuel-rich combustor plays a central role in the improvement of thermal efficiency.

To develop the pressurized and fuel-rich combustor for the proposed system, it is necessary to understand the turbulent combustion characteristics in detail. We have performed a numerical simulation based on a new concept to predict the turbulent combustion characteristics of a methane–air diffusion flame. This simulation makes use of two models: the assumed provably density function (PDF) model based on counterflow diffusion flame and the eddy dissipation concept (EDC) model with reduced chemical reaction schemes. The calculated results are compared to the measured data, and the performance of the turbulent combustion simulation is discussed.

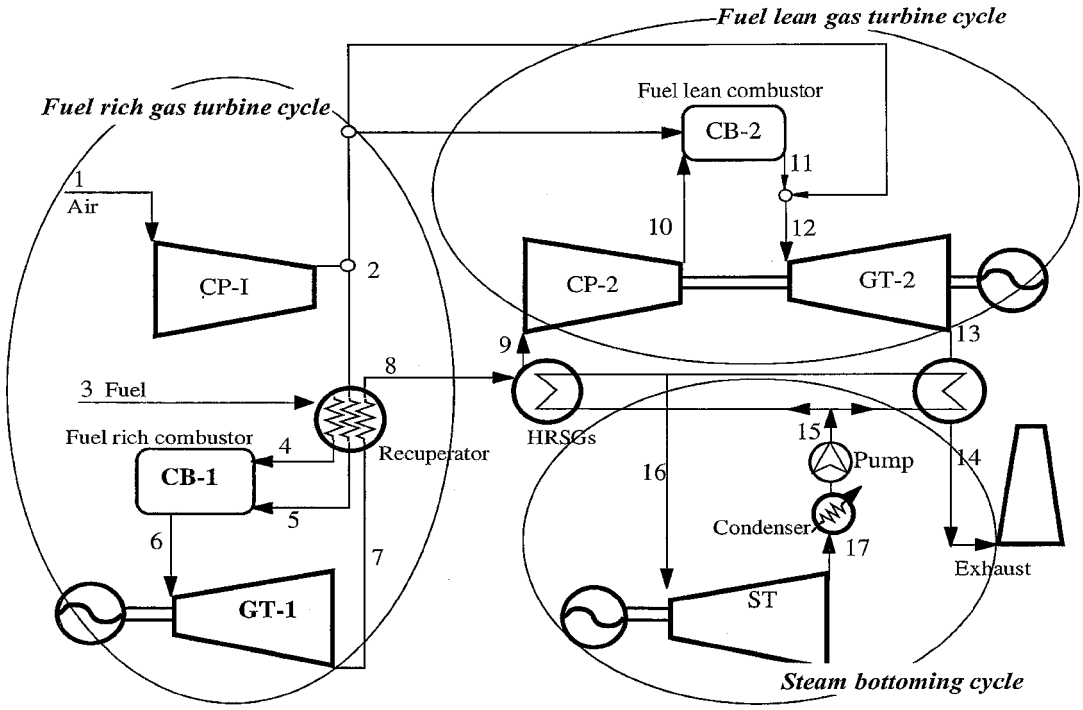

Fig. 1 Schematic diagram of the CGT.

Experimental

The total layout of the experimental setup, including the gas supply system, is shown in Fig. 2a. Air and methane were supplied from gas cylinders connected in parallel. A sequencer and a personal computer controlled the equipment. Figure 2b shows the details of the laboratory-scale combustor employed in this work. It consisted primarily of a injector, an igniter, a combustion chamber, and an exhaust nozzle. The size of the combustor was 50 mm in inner diameter D and 626 mm in length L. The combustor is made of stainless steel with pure copper inside, and the combustor wall is water cooled. The injector is of a coaxial type. Methane was supplied through the inner nozzle of 4 mm in inner diameter, and air was fed through the outer nozzle of the inner diameter of 13 mm. The exhaust throats consisted of five holes 1.7 mm in diameter and four holes 1.0 mm. Both methane and air are introduced into the combustion chamber without swirl, and their feed rates are set to 0.62 and 8.11 kg/hr, respectively. The Reynolds number is 6218 at methane injector outlet. The equivalence ratio is 1.32, and the pressure in the combustion chamber is 1.0 MPa.

Combustion gas and temperature are measured at three positions. Positions A, B, and C were located at 136 ($x/D = 2.7$), 236 ($x/D = 4.7$), and 336 mm ($x/D = 6.7$), respectively, where x is the axial distance and D is the inner diameter of the combustor. At each position, both the thermocouples and the gas sampling probes were set at six points (0, 5, 10, 15, 20, and 25 mm from the center of the combustor) to measure radial profiles of combustion temperature and gas concentration, as shown in Fig. 2c. The thermocouple was the R (Pt/Pt–Rh 16%) type with a 0.1-mm wire diameter. The sampling rate of the temperature measurement is set at 500 Hz taking account of the thermocouple's response time. The gas sampling probes were 1 mm in diameter, and the gas components were measured using a gascromatograph with a thermal conductivity detector (TCD). Figure 3 shows an example of time changes in pressure and temperature during the combustion experiments.[3] Each experiment began by supplying methane; the igniter started to run 2 s later. After 1-s intervals, air was fed. In the experiments, the igniter worked for 6 s. The temperature measurement and combustion gas sampling were done between 10 and 15 s in steady state, as shown in Fig. 3.

Numerical Simulation

In the combustion simulation developed in this study, the k–ε two-equation turbulence model[4] and the six-flux model[5] are used to describe the turbulent flowfield and the radiative heat transfer, respectively.

The general form of the governing equations in three-dimensional cylindrical coordinates is

$$\frac{\partial}{\partial x}(\rho U\phi) + \frac{1}{r}\frac{\partial}{\partial r}(r\rho V\phi) + \frac{1}{r}\frac{\partial}{\partial \theta}(\rho W\phi) = \frac{\partial}{\partial x}\left(\Gamma_\phi \frac{\partial \phi}{\partial x}\right) + \frac{1}{r}\frac{\partial}{\partial r}\left(r\Gamma_\phi \frac{\partial \phi}{\partial r}\right) + \frac{1}{r}\frac{\partial}{\partial \theta}\left(\Gamma\phi \frac{\partial \phi}{r\partial \theta}\right) + S_\phi \tag{1}$$

where ϕ represents the dependent variables that denote the mass (continuity); momentum U, V, and W; turbulence energy k; dissipation rate of energy ε; enthalpy h; radiative heat flux F_x, F_r, and F_θ; mixture fraction f; and variance of mixture fraction g. Γ_ϕ is turbulent exchange coefficient and S_ϕ is a source term. The expressions of Γ_ϕ and S_ϕ are shown in Table 1. In Table 1,

$$\mu_t = C_\mu \rho \frac{k^2}{\varepsilon}, \qquad \mu_{\text{eff}} = \mu_t + \mu \tag{2}$$

$$G_k = \mu_{\text{eff}}\left[2\left\{\left(\frac{\partial U}{\partial x}\right)^2 + \left(\frac{\partial V}{\partial r}\right)^2 + \left(\frac{\partial W}{r\partial \theta} + \frac{V}{r}\right)^2\right\} + \left(\frac{\partial U}{\partial r} + \frac{\partial V}{\partial x}\right)^2 + \left(\frac{\partial W}{\partial x} + \frac{\partial U}{r\partial \theta}\right)^2 + \left(\frac{\partial V}{r\partial \theta} + \frac{\partial W}{\partial r} - \frac{W}{r}\right)^2\right] \tag{3}$$

$$G_g = \mu_{\text{eff}}\left[\left(\frac{\partial \bar{f}}{\partial x}\right)^2 + \left(\frac{\partial \bar{f}}{\partial r}\right)^2 + \left(\frac{\partial \bar{f}}{r\partial \theta}\right)^2\right] \tag{4}$$

$$C_\mu = 0.09, \qquad C_{\varepsilon 1} = 1.44, \qquad C_{\varepsilon 2} = 1.92$$

$$C_{g1} = 2.8, \qquad C_{g2} = 2.0 \tag{5}$$

$$\sigma_k = 1.0, \qquad \sigma_\varepsilon = 1.3, \qquad \sigma_m = 0.9$$

$$\sigma_h = 0.9, \qquad \sigma_f = 0.9, \qquad \sigma_g = 0.9 \tag{6}$$

The discrete equations of the governing equations (1) are derived using power-law scheme[6] and iteratively solved by the SIMPLE

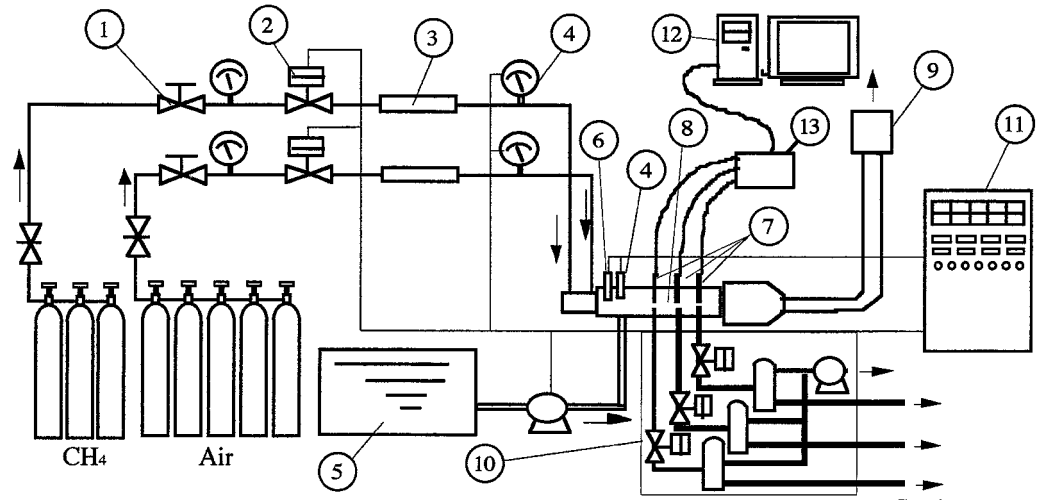

① Control valve
② Stop valve
③ Mass flow meter
④ Pressure transducer
⑤ Water reservoir
⑥ Igniter
⑦ Thermocouple
⑧ Combustor
⑨ Silencer
⑩ Gas sampler
⑪ Console
⑫ Personal computer
⑬ Thermocouple amplifier

a)

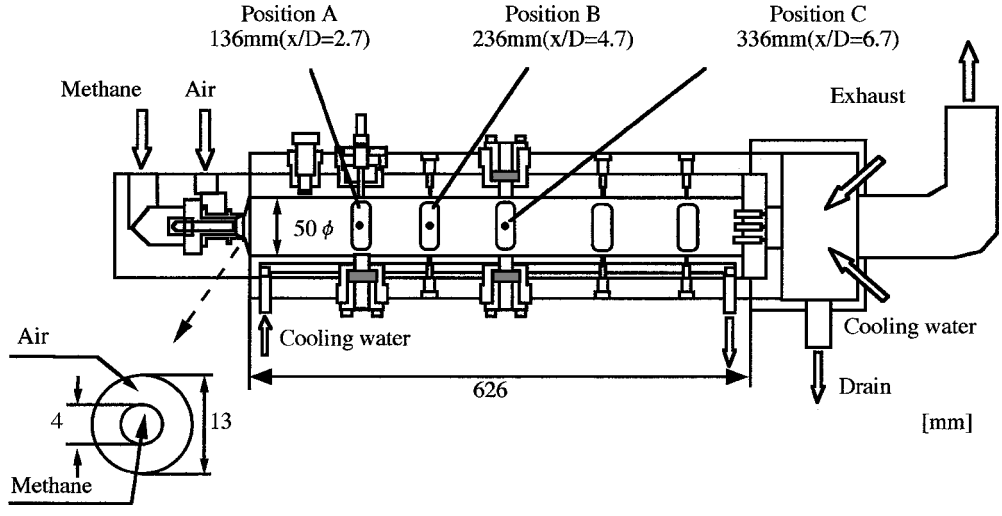

b)

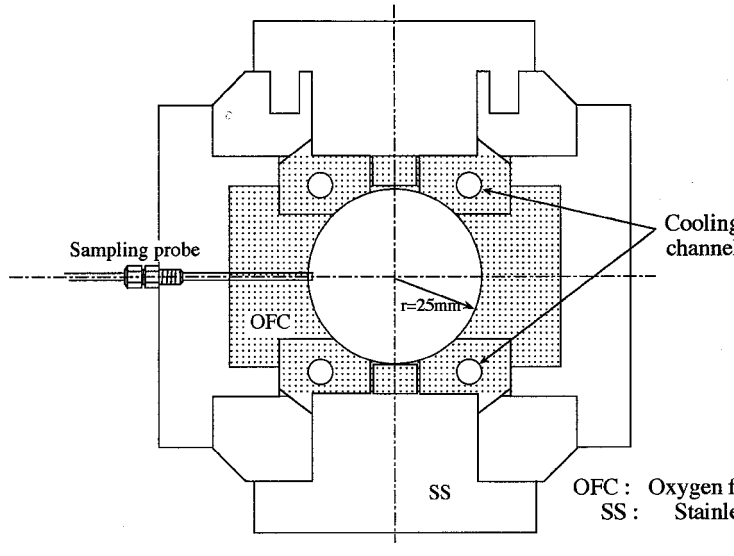

c)

Fig. 2 Experimental apparatus: a) total layout, b) details of the laboratory-scale high-pressure combustor, and c) cross-section of the laboratory-scale combustor.

Table 1 Source terms and turbulent diffusion coefficient for governing equations

ϕ	Γ_ϕ	S_f
1	0	0
U	μ_{eff}	$\frac{\partial}{\partial x}\left(\mu_{\text{eff}}\frac{\partial U}{\partial x}\right)+\frac{1}{r}\frac{\partial}{\partial r}\left(r\mu_{\text{eff}}\frac{\partial V}{\partial r}\right)+\frac{1}{r}\frac{\partial}{\partial \theta}\left(\mu_{\text{eff}}\frac{\partial W}{\partial \theta}\right)-\frac{\partial P}{\partial x}$
V	μ_{eff}	$\frac{\partial}{\partial x}\left(\mu_{\text{eff}}\frac{\partial U}{\partial r}\right)+\frac{1}{r}\frac{\partial}{\partial r}\left(r\mu_{\text{eff}}\frac{\partial V}{\partial r}\right)+\frac{1}{r}\frac{\partial}{\partial \theta}\left[r\mu_{\text{eff}}\frac{\partial}{\partial r}\left(\frac{W}{r}\right)\right]-2\frac{\mu_{\text{eff}}}{r}\left(\frac{\partial W}{r\partial\theta}+\frac{V}{r}\right)+\frac{\rho W^2}{r}-\frac{\partial P}{\partial r}$
W	μ_{eff}	$\frac{\partial}{\partial x}\left(\mu_{\text{eff}}\frac{\partial U}{r\partial\theta}\right)+\frac{\mu_{\text{eff}}}{r}\left[r\frac{\partial}{\partial r}\left(\frac{W}{r}\right)+\frac{1}{r}\frac{\partial V}{\partial\theta}\right]+\frac{1}{r}\frac{\partial}{\partial r}\left[r\mu_{\text{eff}}\left(\frac{1}{r}\frac{\partial V}{\partial\theta}-\frac{W}{r}\right)\right]+\frac{1}{r}\frac{\partial}{\partial\theta}\left[\mu_{\text{eff}}\left(\frac{\partial W}{r\partial\theta}+\frac{2V}{r}\right)\right]-\rho\frac{VW}{r}-\frac{\partial P}{r\partial\theta}$
k	$\frac{\mu_{\text{eff}}}{\sigma_k}$	$G_k-\rho\varepsilon$
ε	$\frac{\mu_{\text{eff}}}{\sigma_\varepsilon}$	$\frac{\varepsilon}{k}(C_{\varepsilon1}G_k-C_{\varepsilon2}\rho\varepsilon)$
m_i	$\frac{\mu_{\text{eff}}}{\sigma_m}$	R_i
h	$\frac{\mu_{\text{eff}}}{\sigma_h}$	$2a_R(F_x+F_r+F_\theta-3E)$
f	$\frac{\mu_{\text{eff}}}{\sigma_f}$	0
g	$\frac{\mu_{\text{eff}}}{\sigma_g}$	$C_{g1}G_g-C_{g2}\rho\frac{\varepsilon}{k}$

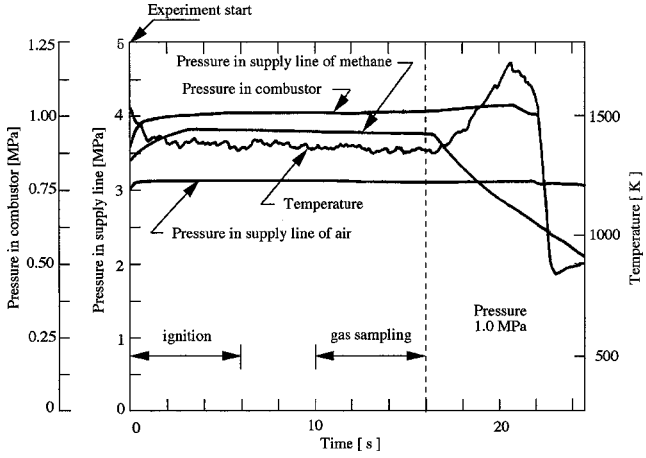

Fig. 3 Example of time changes in pressure and temperature during combustion.[3]

algorithm with TDMA.[6] The three-dimensional cylindrical finite difference grid employed here has $55 \times 32 \times 4$ grid nodes in the axial, radial, and angular directions, respectively. The gas flow characteristics at the wall boundary are estimated using the wall function model. The inlet conditions such as air velocity, components, temperature, and gas composition are also given by the experimental condition. The soot formation was not included in this study because we considered that its influence would be small and would not affect our simulation result. Recent experimental data from Beltrame et al.[7] and our research show that the formation of soot in the fuel-rich methane combustion has little effect on temperature and gas composition.

Assumed PDF Model

In this study, the assumed PDF model was employed to estimate the formation of combustible chemical species such as CO an H_2 under the fuel-rich condition. This model can be considered as an extension of the flame sheet model that assumes an infinitely fast chemical reaction such that the reaction zone is an infinitely thin interface. That is, the microscopic structure of turbulent diffusion flames can be expressed in one dimension. This study calculated such a flame structure by use of a numerical simulation of a counterflow diffusion flame. With the equal diffusivity assumption, under constant pressure combustion without heat loss, the thermochemical properties are determined completely by the local mixing state, which is described by the conserved scalar. In this model, a mixture fraction is used as the conserved scalar and is expressed as follows[8–10]:

$$f = (Z_i - Z_{i2})/(Z_{i1} - Z_{i2}) \tag{7}$$

The mixture fraction is locally varying in the turbulent flame. Here, we assumed PDF to describe the probability of the mixture fraction at each local position. Clipped Gaussians were employed as the shapes of PDF. The clipped Gaussians are characterized by using f and g. Details of the clipped-Gaussian function are given in Appendix A. The relationships between the mixture fraction and mass fraction of the chemical species were given by the calculated results of the counterflow diffusion flame. Finally, the mean mass fraction of the chemical species is

$$\bar{m}_i = \int_0^1 m_i(f) \times P(f)\,\mathrm{d}f \tag{8}$$

For the assumed PDF model, each local composition is decided by the relationship between the local value of mixture fraction f and its variance g. This relationship is called the library. Therefore, the assumed PDF model needs what constructs the library from numerical simulations or experimental data, before the actual numerical simulation for turbulent combustion field. The numerical simulation of a one-dimensional couterflow diffusion flame was employed to construct the library, and the details will be explained in the next section.

Calculation of Counterflow Diffusion Flame

Figure 4 shows the analysis model for the counterflow diffusion flame.[11] Methane and air jet planes are at intervals of L. Each plane is infinitely wide in the y and z directions. Methane and air are supplied at $x = 0$ and L, respectively. In this numerical simulation, L is set to 15 mm, and the number of differential grids in computational domain is 201. The initial temperature of methane and air is 298 K. Table 2 shows the chemical species and elementary reactions using the calculation for the counterflow diffusion flame. We consider 16 chemical species and 25 elementary reactions. Thermodynamic data for chemical reactions are quoted from the CHEMKIN database.[12] Transportational coefficients are calculated by the simplified transport model. Figure 5 shows the calculated results for the counterflow

Table 2 Chemical species and elementary reactions used in the calculation of counterflow diffusion flame

Number	Reaction	Number	Reaction
R1	$H + O_2 \Leftrightarrow OH + O$	R14	$CH_2O + H \Rightarrow HCO + H_2$
R2	$O + H_2 \Leftrightarrow OH + O$	R15	$CH_2O + OH \Rightarrow HCO + H_20$
R3	$H_2 + OH \Leftrightarrow H_2O + H$	R16	$HCO + H \Rightarrow CO + H_2$
R4	$OH + OH \Leftrightarrow O + H_2O$	R17	$HCO + M \Rightarrow CO + H + M$
R5	$H + O_2 + M \Rightarrow HO_2 + M$	R18	$CH_3 + O_2 \Rightarrow CH_3O + O$
R6	$H + HO_2 \Rightarrow OH + OH$	R19	$CH_3O + H \Rightarrow CH_2O + H_2$
R7	$H + HO_2 \Rightarrow H_2 + O_2$	R20	$CH_3O + M \Rightarrow CH_2O + H + M$
R8	$OH + HO_2 \Rightarrow H_2O + O_2$	R21	$HO_2 + HO_2 \Rightarrow H_2O_2 + O_2$
R9	$CO + OH \Leftrightarrow CO_2 + H$	R22	$H_2O_2 + M \Leftrightarrow OH + OH + M$
R10	$CH_4 + (M) \Leftrightarrow CH_3 + H + (M)$	R23	$H_2O_2 + OH \Leftrightarrow H_2O + HO_2$
R11	$CH_4 + H \Leftrightarrow CH_3 + H_2$	R24	$OH + H + M \Rightarrow H_2O + M$
R12	$CH_4 + OH \Leftrightarrow CH_3 + H_2O$	R25	$H + H + M \Rightarrow H_2 + M$
R13	$CH_3 + O \Rightarrow CH_2O + H$	——	——

[a] CH_4, O_2, N_2, CO_2, H_2O, H, O, OH, HO_2, H_2, CO, H_2O_2, HCO, CH_2O, CH_3, and CH_3O.

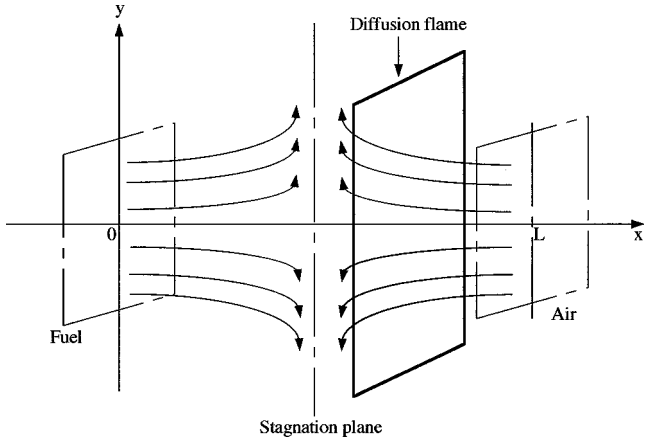

Fig. 4 Theoretical model of counterflow diffusion flame.

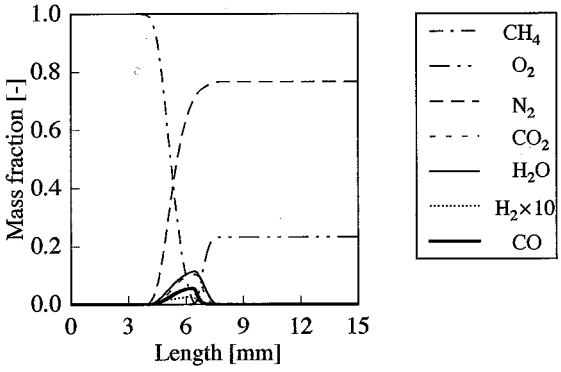

Fig. 5 Calculated results for counterflow diffusion flame.

diffusion flame. From this, it is clear that the combustion reaction zone exists from $x = 3$ to 8 mm. In Fig. 5, the axis of L is converted into a mixture fraction by means of Eq. (2). The converted result is shown in Fig. 6. The species concentrations corresponding to the value of f are predicted from these results. Moreover, temperature profiles in the combustor are calculated by the composition of the combustion gas in each local grid.

When an actual turbulent combustion field is numerically simulated, as shown in following section, the mixture fraction f and its variance g are predicted in the flowfield calculation [Eq. (1)]. Subsequently, the concentrations of chemical species in each local position are calculated using the library. As stated earlier, one of the features of the assumed PDF model is that it separates the calculation of the combustion reaction from that of the flowfield.

Multistep EDC Model

We also performed numerical simulations that employ the EDC model[13] based on reduced reaction schemes for methane combustion

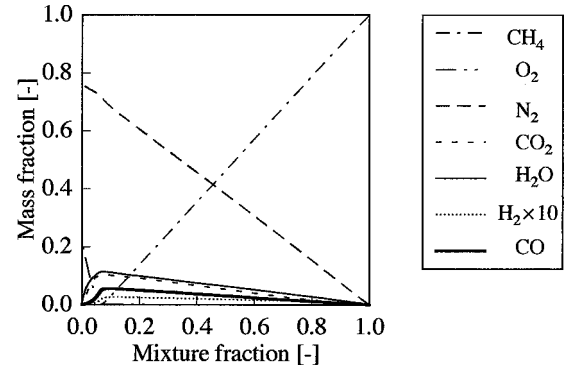

Fig. 6 Relationship between mixture fraction and mass fraction of chemical species.

as a comparison for the reaction model. We abbreviate the simulation of one-step, three-step, and four-step reduced reaction schemes as one-step EDC, three-step EDC, and four-step EDC, respectively.

The reduced reaction schemes for each EDC consist of the following reactions.[14–16]

One step:

$$CH_4 + 2O_2 \longrightarrow CO_2 + 2H_2O \tag{9}$$

Three step:

$$CH_4 + O_2 \longrightarrow CO + H_2 + H_2O \tag{10}$$

$$CO + H_2O \longleftrightarrow CO_2 + H_2 \tag{11}$$

$$H_2 + \tfrac{1}{2}O_2 \longrightarrow H_2O \tag{12}$$

Four step:

$$CH_4 + \tfrac{1}{2}O_2 \longrightarrow CO + 2H_2 \tag{13}$$

$$CH_4 + H_2O \longrightarrow CO + 3H_2 \tag{14}$$

$$CO + H_2O \longleftrightarrow CO_2 + H_2 \tag{15}$$

$$H_2 + \tfrac{1}{2}O_2 \longrightarrow H_2O \tag{16}$$

Three-step and four-step EDC models are able to estimate CO and H_2 concentrations by taking into account water-, gas-, and hydrogen-forming reactions. The procedures to obtain the reduced mechanisms are given in Appendix B.

Boundary Conditions

The boundary conditions are shown in Table 3. The gas flow at the wall boundary is characterized using the wall function model, and the temperature of the inner wall of the combustor is estimated by solving the heat balance equation for the combustor wall. The

Table 3 Boundary conditions

ϕ	Symmetrical axis	Wall	Outlet plane
U	$\frac{\partial U}{\partial r}=0$	Wall function	$\frac{\partial U}{\partial x}=0$
V	0	Wall function	$\frac{\partial V}{\partial x}=0$
W	$\frac{\partial W}{\partial r}=0$	Wall function	$\frac{\partial W}{\partial x}=0$
k	$\frac{\partial k}{\partial r}=0$	Wall function	$\frac{\partial k}{\partial x}=0$
ε	$\frac{\partial \varepsilon}{\partial r}=0$	Wall function	$\frac{\partial \varepsilon}{\partial x}=0$
h	$\frac{\partial h}{\partial r}=0$	Heat balance for wall	$\frac{\partial h}{\partial x}=0$
$f(m_i)$	$\frac{\partial f}{\partial r}=\frac{\partial m_i}{\partial r}=0$	$\frac{\partial m_i}{\partial n}=0$	$\frac{\partial m_i}{\partial x}=0$

heat conduction of the wall and heat flux transported to the inner wall by convection and radiation are considered in the equation. The temperature of the outer wall was assumed to be constant (<373 K) because of the water cooling. The inlet conditions such as methane and air velocity component, temperature, and equivalence ratio are given by the experimental conditions.

Results and Discussion

Thermocouples were calibrated before each experiment, and the radiative heat transfer of the thermocouple was taken into account. The fluctuations of the species concentrations and temperature data were within 5% in the experiments. Figure 7 show the comparisons between the calculated and measured radial and axial profiles of temperature. The radial profile of temperature at position A calculated by the assumed PDF model is good compared to the measured data. On the other hand, the predicted result for one-step EDC is overestimated and for four-step EDC is underestimated. It seems that, for one-step EDC, all products are evaluated as CO_2 and H_2O and that four-step EDC is affected by the steam reforming reaction (9), which is an endothermic reaction. At position B, only one-step EDC is overestimated; the others show good agreement. Moreover, at also position C, the tendency of measured temperature, which falls gradually at $r/D > 0.4$, is predicted by all of the simulations. When the centerline ($r/D = 0$) between calculated and measured axial profiles of temperature is examined, it is clear that one-step EDC model must overestimate the temperature profile in the entire combustor. On the other hand, both three- and four-step EDC models show the tendency of a temperature rise in the upstream region of the combustor along with the experimental result.

Figure 8 shows the comparison between calculated and measured profiles of CO mole fraction. At both positions A and C, the radial profiles calculated by the assumed PDF model conform to the measured one. At position C, the CO profile calculated by four-step EDC appears to be almost the same as that by three-step EDC. However, both three-step and four-step EDC are underestimated near the combustor wall ($r/D = 0.4$). It seems that the equilibrium represented by reactions (6) and (10) shifts to the right-hand side in those regions. From the discussions of the centerline profile between the calculation and the measurement, results of all models show good agreement with experimental ones.

Figure 9 shows the comparisons between calculated and measured radial and axial profiles of the H_2 mole fraction at each point. The radial profile calculated by each model is comparable to the measured data at position A. At both positions B and C, however, the predicted profiles are low compared with the measured one. For three-step and four-step EDC, these discrepancies result because that we have not taken into account the equilibrium states for reactions (7) or (11). For assumed PDF model, it is inferred that this discrepancy is mainly caused by the adiabatic approximation in the counterdiffusion flame. From the comparison on the axial profiles,

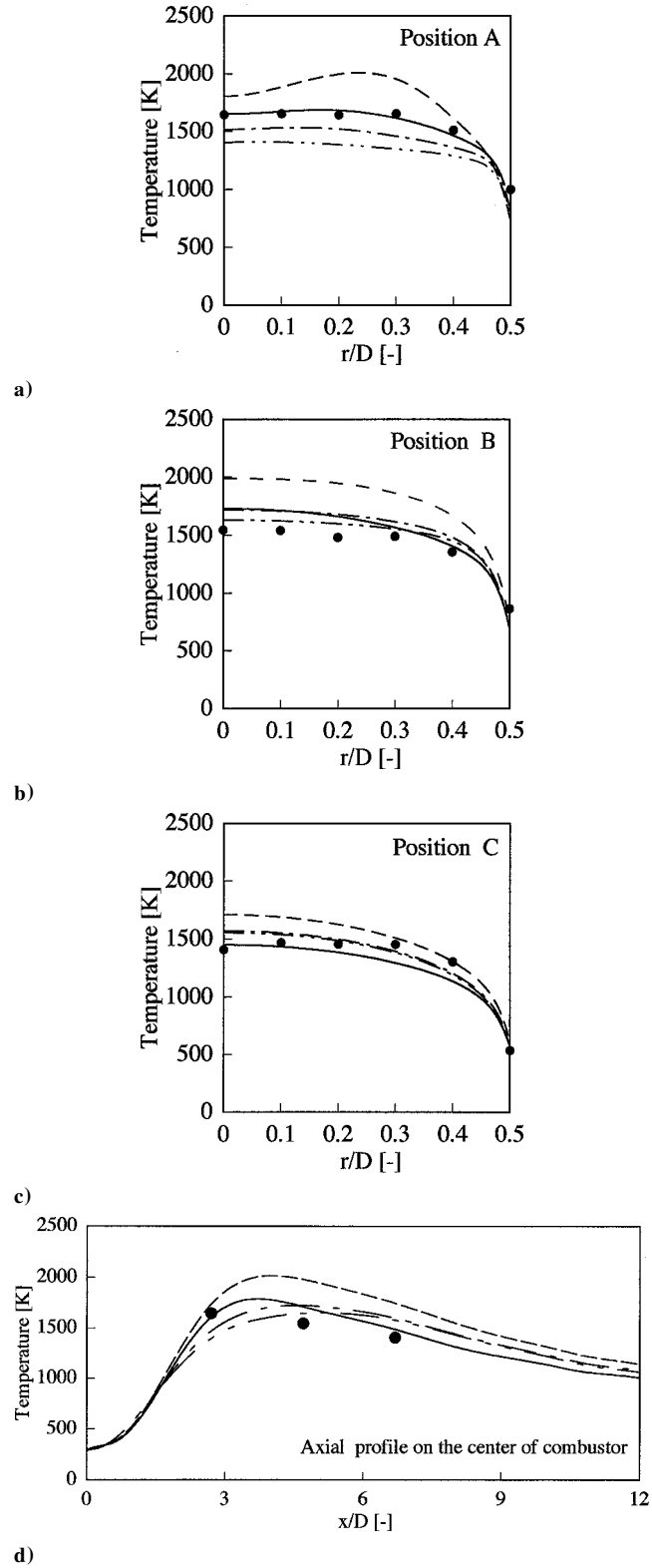

Fig. 7 Comparison of temperature profiles between experimental and simulated results: . . . , experimental data; ——, assumed PDF; – – –, one-step EDC; –·–, three-step EDC; and –···–, four-step EDC.

both assumed PDF and four-step EDC models must underestimate the H_2 profile. The three-step EDC model shows the peak on the upstream region, although no peaks were measured in the experiment. These discrepancies require further investigation in the fuel-rich combustion simulation.

Because computation times and CPU loads are significant problems in modeling the turbulent combustor, we investigated the times needed for the turbulent combustion models developed in this study.

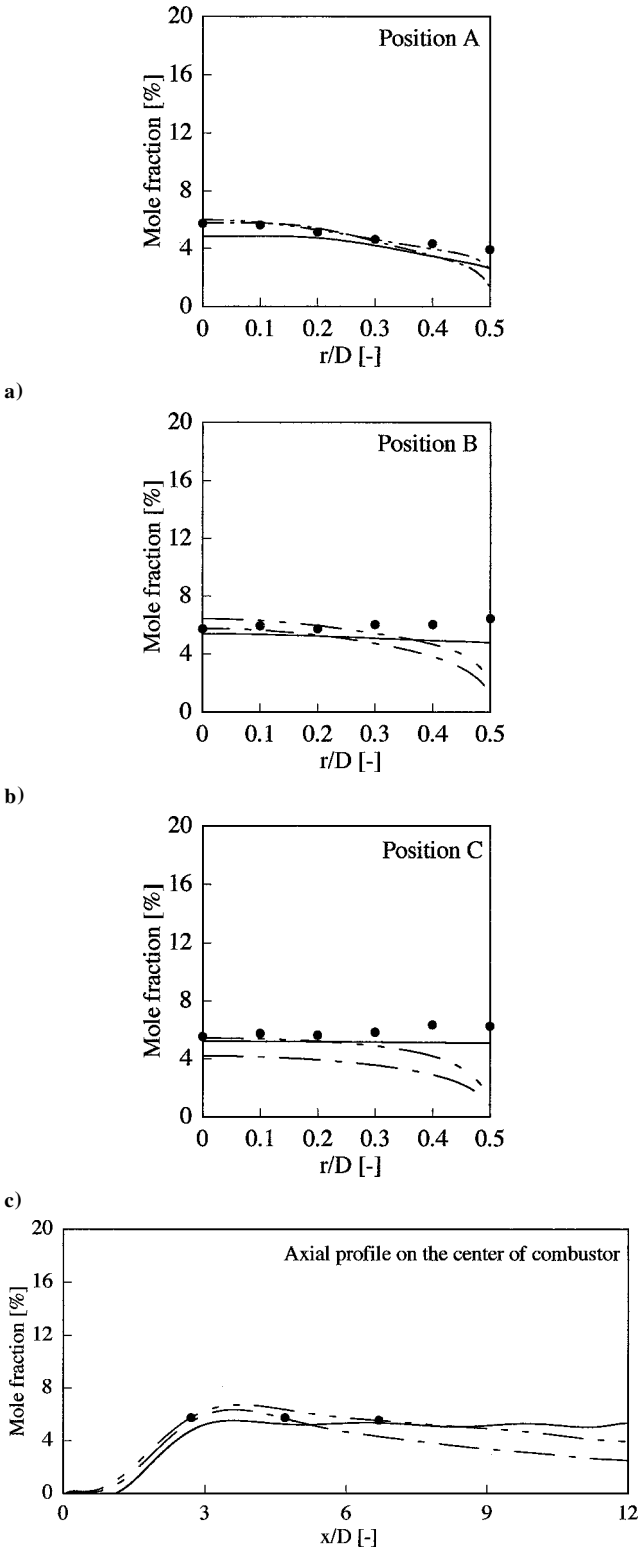

Fig. 8 Comparison of CO profiles between experimental and simulated results: . . . , experimental data; ——, assumed PDF; –·–, three-step EDC; and –···–, four-step EDC.

The described numerical simulations were carried out using a commonly used workstation DEC 500au as a calculation computer. Computational times for the combustion simulations in each simulation model were within 12 h, as shown in Table 4. Direct numerical simulation (DNS)[17] and other turbulent combustion models, such as the reaction progress variable model[17] and the second moment closure model,[18] have a much larger CPU load and longer computational time, for example, the DNS computational time for the laminar

Table 4 Results of calculation time in PDF and EDC models

Reaction model	Computational time, h
One-step EDC	6.0
Three-step EDC	7.0
Four-step EDC	8.0
Assumed PDF	12.0

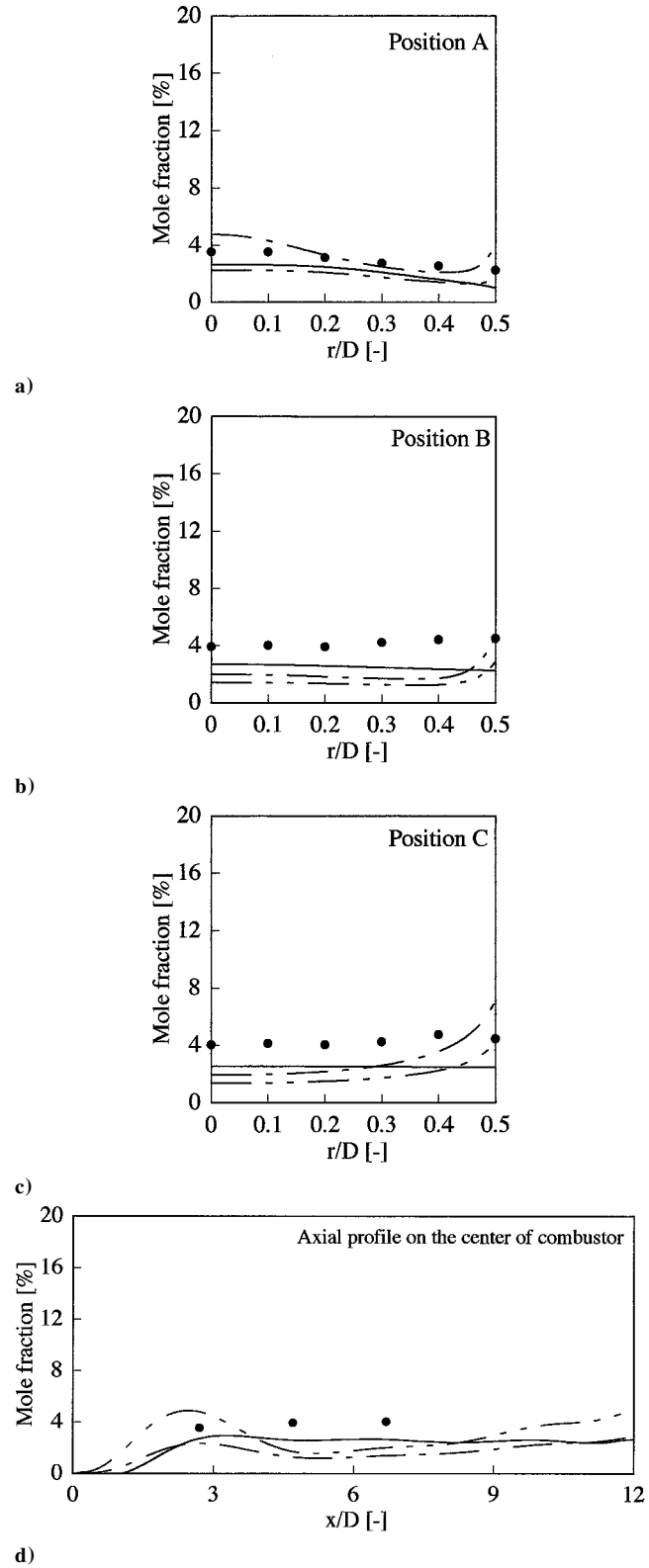

Fig. 9 Comparison of H_2 profiles between experimental and simulated results: . . . , experimental data; ——, assumed PDF; –·–, three-step EDC; and –···–, four-step EDC.

hydrogen diffusion flame calculation is more than one month. Therefore, we concluded that the turbulent combustion models developed in this study have a great advantage in practical application.

Conclusions

Turbulent combustion simulation under high-pressure and fuel-rich conditions was performed. An assumed PDF model based on a counterflow diffusion flame and EDC models based on a reduced reaction scheme were newly employed as fuel-rich combustion reaction models. The calculated results were compared with the measured results in detail. From the results and discussion, it was clear that the assumed PDF model could be the most reasonable for estimating temperature profiles. It was obvious that each model underestimates H_2 profiles compared with the measured results. Enhancement of the accuracy of H_2 prediction is a future task in the fuel-rich combustion simulation. Among the combustion models studied here, the assumed PDF model showed good agreement with measurement results in CO profiles. Furthermore, times needed for the combustion simulation were investigated. All turbulent combustion models could finish the calculation within 12 h. Because other combustion models, such as DNS and second moment closer models, have a much larger CPU load and longer calculation time, we concluded that these combustion models, especially the assumed PDF model, were suitable to practical application for developing the fuel-rich combustor of the CGT system.

Appendix A: PDF

In this study, the clipped-Gaussian distribution function is used as the PDF of the scalar calculation.[8–10] The clipped-Gaussian distribution function is expressed as

$$P(f) = \frac{1}{\sigma\sqrt{2\pi}} \exp\left[-\frac{1}{2}\left(\frac{f-\mu}{\sigma}\right)^2\right][H(f) - H(f-1)] + A\delta(0) + B\delta(0) \tag{A1}$$

where μ and σ are an average and a variance of the clipped-Gaussian distribution. $H(f)$ is a heaviside function. A and B are calculated as

$$A = \int_{-\infty}^{1} \frac{1}{\sigma\sqrt{2\pi}} \exp\left[-\frac{1}{2}\left(\frac{f-\mu}{\sigma}\right)^2\right] \mathrm{d}f \tag{A2}$$

$$B = \int_{1}^{\infty} \frac{1}{\sigma\sqrt{2\pi}} \exp\left[-\frac{1}{2}\left(\frac{f-\mu}{\sigma}\right)^2\right] \mathrm{d}f \tag{A3}$$

whereas μ and σ are calculated using the mixture fraction f and its variance g:

$$f = 1 + (\mu - 1)F(z_1) - \mu F(Z_0) + \sigma^2/2\pi\left[\exp\left(-\tfrac{1}{2}z_0^2\right) - \exp\left(-\tfrac{1}{2}z_1^2\right)\right] \tag{A4}$$

$$g = 1 + (\sigma^2 + \mu^2 - 1)F(z_1) - (\mu^2 + \sigma^2)F(Z_0) + \sigma^2/2\pi\left[Z_0\exp\left(-\tfrac{1}{2}Z_0^2\right) - Z_1\exp\left(-\tfrac{1}{2}Z_1^2\right)\right] + 2\sigma\mu\Big/\sqrt{2\pi}\left[Z_0\exp\left(-\tfrac{1}{2}Z_0^2\right) - Z_1\exp\left(-\tfrac{1}{2}Z_1^2\right)\right] - f^2 \tag{A5}$$

In the actual turbulent combustion simulation, the clipped-Gaussian PDF is estimated in each grid cell by means of the mixture fraction f and its variance g.

Appendix B: Reduced Reaction Scheme for EDC Model

This paper employed two reduced reaction schemes for EDC model: three-step and four-step reduced mechanisms. The details of the derivation are given in Refs. 14–16. The reduced schemes were estimated as follows.

It has been shown that the oxidation of methane can be represented by following four global reactions[15]:

$$CH_4 + 2H + H_2O \longrightarrow CO + 4H_2 \tag{B1}$$

$$CO + H_2O \longleftrightarrow CO_2 + H_2 \tag{B2}$$

$$H + H + M \longrightarrow H_2 + M \tag{B3}$$

$$O_2 + 3H_2 \longleftrightarrow 2H + 2H_2O \tag{B4}$$

The preceding set of reactions was deduced systematically from the detailed chemical kinetic mechanism of oxidation of methane shown in Table B1. The reaction rates are as follows.

$$w_I = w34a + w34b - w44a + w44b + w47a - w47b + w48a - w48b + w49a - w49b + w50a - w50b + w51a - w51b \tag{B5}$$

$$w_{II} = w20a - w20b + w21a - w21b + w22a - w22b + w23a - w23b + w26a - w26b - w38 - w42 \tag{B6}$$

$$w_{III} = w5a - w5b + w6a - w6b + w7a - w7b + w8a - w8b + w15a - w15b + w22a - w22b + w24a - w24b + w25a - w25b + w26a - w26b + w27a - w27b + w28a - w28b - w35a + w35b - w37a + w37b - w38 + w39a - w39b + w44a - w44b - w46a + w46b \tag{B7}$$

$$w_{IV} = w1a - w1b - w7a + w7b + w9a - w9b + w11a - w11b + w14 - w16a + w16b - w18a + w18b - w19a + w19b + w21a - w21b + w23a - w23b + w33a - w33b + w37a - w37b + w41 + w42 + w50a - w50b \tag{B8}$$

where the numbers in the Eqs. (B5–B7) refer to the reaction numbers of Table B1 and a and b indicate forward and backward reactions, respectively.

To reduce the chemical kinetic mechanism even further, we shall assume that the concentration of the hydrogen radicals is in steady state everywhere except in the combustion field. As a consequence of this additional steady-state approximation, we obtain the relation

$$w_{IV} = w_I + w_{III} \tag{B9}$$

The consideration of Eq. (B5), the correlation between Eqs. (B1) and (B3), and the correlation among Eqs. (B1–B3) reduces the four-step mechanism [Eqs. (B1–B4)] to the three-step mechanism used in this paper:

$$CH_4 + O_2 \longrightarrow CO + H_2 + H_2O \tag{B10}$$

$$CO + H_2O \longleftrightarrow CO_2 + H_2 \tag{B11}$$

$$H_2 + \tfrac{1}{2}O_2 \longrightarrow H_2O \tag{B12}$$

The fuel breakdown reaction becomes remarkable in a high-temperature condition. Regarding the fuel breakdown reactions, which broadly determine the shape of the primary reaction zone, it is well known that initial attack on the fuel is made predominantly by hydroxyl and hydrogen radicals, and that subsequently, in higher alkanes, thermal decomposition is of major importance. Seshadori and Peters showed a fuel breakdown reaction involving water and the hydrogen radical from the sensitivity analysis of the detailed reaction mechanism[14]:

$$CH_4 + 2H + H_2O \longleftrightarrow CO + H_2 \tag{B13}$$

Table B1 Detailed reaction mechanism for modeling reduced reaction scheme[13,14]

Number	Reaction	Number	Reaction
R1	$O_2 + \Leftrightarrow OH + O$	R27	$CHO + H \Leftrightarrow CO + H_2$
R2	$H_2 + O \Leftrightarrow OH + H$	R28	$CHO + O \Leftrightarrow CO + OH$
R3	$OH + OH \Leftrightarrow H_2O + H$	R29	$CHO + O \Leftrightarrow CO_2 + H$
R4	$OH + OH \Leftrightarrow H_2O + O$	R30	$CHO + OH \Leftrightarrow CO + H_2O$
R5	$H + O_2 + M' \Leftrightarrow HO_2 + M'$	R31	$CHO + O_2 \Leftrightarrow CO + HO_2$
R6	$HO_2 + H \Leftrightarrow OH + OH$	R32	$CHO + M' \Leftrightarrow CO + H + M'$
R7	$HO_2 + H \Leftrightarrow H_2 + O_2$	R33	$CH_2 + H \Leftrightarrow CH + H_2$
R8	$HO_2 + OH \Leftrightarrow H_2O + O_2$	R34	$CH_2 + O \Rightarrow CO + H + H$
R9	$HO_2 + H \Leftrightarrow H_2O + O$	R35	$CH_2 + O_2 \Rightarrow CO + OH + H$
R10	$HO_2 + O \Rightarrow OH + O_2$	R36	$CH_2 + O_2 \Rightarrow CO_2 + H_2$
R11	$HO_2 + HO_2 \Rightarrow H_2O_2 + O_2$	R37	$CH_2O + H \Leftrightarrow CHO + H_2$
R12	$OH + OH + M' \Leftrightarrow H_2O_2 + M'$	R38	$CH_2O + O \Leftrightarrow CHO + OH$
R13	$H_2O_2 \Leftrightarrow H_2O + OH$	R39	$CH_2O + OH \Leftrightarrow CHO + H_2O$
R14	$H_2O_2 + OH \Leftrightarrow H_2O + HO_2$	R40	$CH_2O + HO_2 \Leftrightarrow CHO + H_2O_2$
R15	$H_2O_2 + H \Leftrightarrow H_2 + HO_2$	R41	$CH_2O + CH_3 \Leftrightarrow CHO + CH_4$
R16	$H_2O_2 + O \Leftrightarrow OH + HO_2$	R42	$CH_2O + M' \Leftrightarrow CHO + H + M'$
R17	$H + H + M' \Leftrightarrow H_2 + H'$	R43	$CH_3 + H \Leftrightarrow CH_2 + H_2$
R18	$H + OH + M' \Leftrightarrow H_2O + M'$	R44	$CH_3 + H \Leftrightarrow CH_4$
R19	$O + O + M' \Leftrightarrow O_2 + M'$	R45	$CH_3 + O \Leftrightarrow CH_2O + H$
R20	$CO + OH \Leftrightarrow CO_2 + H$	R46	$CH_3 + M \Leftrightarrow CH_2 + H + M$
R21	$CO + HO_2 \Leftrightarrow CO_2 + OH$	R47	$CH_4 + H \Leftrightarrow CH_3 + H_2$
R22	$CO + O + M' \Leftrightarrow CO_2 + M'$	R48	$CH_4 + O \Rightarrow CH_3 + OH$
R23	$CO + O_2 \Leftrightarrow CO_2 + O$	R49	$CH_4 + OH \Leftrightarrow CH_3 + H_2O$
R24	$CH + O \Leftrightarrow CO + H$	R50	$CH_4 + HO_2 \Leftrightarrow CH_3 + H_2O_2$
R25	$CH + O_2 \Leftrightarrow CHO + O$	R52	$CH_4 + CH_2 \Leftrightarrow CH_3 + CH_3$
R26	$CH + CO_2 \Leftrightarrow CHO + CO$	——	M, M′: third body

Likewise, significant reactions are shown as follows:

$$H + O_2 \longleftrightarrow OH + O \tag{B14}$$

$$CO + OH \longleftrightarrow CO_2 + H \tag{B15}$$

$$O + H_2 \longleftrightarrow OH + H \tag{B16}$$

$$OH + OH \longleftrightarrow H_2O + H \tag{B17}$$

$$OH + H_2 \longleftrightarrow H_2O + H \tag{B18}$$

Using the same procedure as in the three-step reduced mechanism, we then obtain four-step reduced mechanism for methane combustion:

$$CH_4 + \tfrac{1}{2}O_2 \longrightarrow CO + 2H_2 \tag{B19}$$

$$CH_4 + H_2O \longrightarrow CO + 3H_2 \tag{B20}$$

$$CO + H_2O \longleftrightarrow CO_2 + H_2 \tag{B21}$$

$$H_2 + \tfrac{1}{2}O_2 \longrightarrow H_2O \tag{B22}$$

References

[1]Arai, N., Teramae, N., and Kobayashi, N., "Challenge for Development of High Efficient Gas Turbine System: The Chemical Gas Turbine System," *Energy World*, Vol. 1, No. 226, 1995, pp. 16, 17.

[2]Furuhata, T., Miyazaki, T., Kobayashi, N., Arai, N., Bujar, D., Tanno, S., and Miura, T., "Combustion Characteristics of Pressurized Methane/Air Combustor for Chemical Gas Turbine System," *Proceedings of 11th International Heat Transfer Conference*, KSME, Seoul, 1998, pp. 282–288.

[3]Yamamoto, T., Miyazaki, T., Furuhata, T., Arai, N., Kobayashi, N., and Miura, T., "Temperature Profile in the Pressurized Methane–Air Combustion," *Journal of Flow Visualization and Image Processing*, Vol. 5, No. 1, 1998, pp. 51–62.

[4]Launder, B. E., "The Prediction of Laminarization with a Two-Equation Model of Turbulence," *International Journal of Heat and Mass Transfer*, Vol. 15, No. 1, 1972, pp. 301–306.

[5]Patanker, S. V., and Spalding, D. B., "A Computer Model for Three-Dimensional Flow in Furnaces," *Proceedings of Fourteenth International Symposium on Combustion*, Vol. 1, Combustion Inst., Pittsburgh, PA, 1973, pp. 605–614.

[6]Patanker, S. V., "Numerical Heat Transfer and Fluid Flow," Hemisphere, New York, 1980, pp. 136–139.

[7]Beltrame, A., Porshnev, P., Merchan, M. W., and Saveliev, A., "Soot and NO Formation in Methane/Air Diffusion Flames," *Combustion and Flame*, Vol. 123, No. 1–2, 2001, pp. 295–310.

[8]Liew, S. K., Bray, K. N. C., Moss, J. B., "A Flamelet Model of Turbulent Non-Premixed Combustion," *Combustion and Flame*, Vol. 27, No. 1, 1981, pp. 69–73.

[9]Buriko, Y. Y., Kuznetsov, V. R., Volkov, D. V., and Zaitsev, S. A., "A Test of a Flamelet Model for Turbulent Nonpremixed Combustion," *Combustion and Flame*, Vol. 96, No. 1, 1994, pp. 104–120.

[10]Chou, C. P., Chen, J. Y., and Yam, C. G., "Numerical Modeling of NO Formation in Laminar Bunsen Flames—A Flamelet Approach," *Combustion and Flame*, Vol. 114, No. 3–4, 1998, pp. 420–435.

[11]Yamashita, H., Nishioka, M., and Takeno, T., "Prediction of NOx Production Rate in the Turbulent Diffusion Flame," *Energy Conversion and Management*, Vol. 38, No. 5, 1997, pp. 1343–1352.

[12]Fisher, E. M., and Koshland, C. P., "Numerical Simulation of the Thermal Destruction of Some Chlorinated C1 and C2 Hydrocarbons," *Journal of the Air and Waste Management*, Vol. 46, No. 10, 1990, pp. 1384–1390.

[13]Magnussen, B. F., and Hjertager, B. H., "On Mathematical Modeling of Turbulent Combustion with Special Emphasis on Soot Formation and Combustion," *Proceedings of the Sixteenth International Symposium on Combustion*, Vol. 1, Combustion Inst., Pittsburgh, PA, 1976, pp. 719–729.

[14]Seshadori, K., and Peters, N., "Asymptotic Structure and Extinction of Methane-Air Diffusion Flames," *Combustion and Flame*, Vol. 73, No. 1, 1988, pp. 23–44.

[15]Jones, W. P., and Lindstedt, R. P., "Global Reaction Schemes for Hydrocarbon Combustion," *Combustion and Flame*, Vol. 73, No. 3–4, 1988, pp. 233–249.

[16]Makita, T., Miyazaki, T., Furuhata, T., and Arai, N., "Turbulent Combustion Characteristics of a Pressurized Methane–Air Combustion Under Fuel Rich Conditions," *Proceedings of International Joint Power Generation Conference*, Vol. 1, ASME, New York, 2000, p. 231.

[17]Swaminathan, N., and Bilger, W., "Assessment of Combustion Submodels for Turbulent Nonpremixed Hydrocarbon Flames," *Combustion and Flame*, Vol. 116, No. 4, 1999, pp. 519–545.

[18]Klimenko, A. Y., and Bilger, W., "Conditional Moment Closure for Turbulent Combustion," *Progress in Energy and Combustion Science*, Vol. 25, No. 6, 1999, pp. 595–687.